Pergamon

Cement and Concrete Research 32 (2002) 1567–1585

CEMENT AND CONCRETE RESEARCH

A discrete crack approach to normal/shear cracking of concrete

J.C. Gálvez[a,*], J. Červenka[b], D.A. Cendón[c], V. Saouma[d]

[a]ETS Ingenieros de Caminos, Universidad de Castilla-La Mancha, Av. Camilo José Cela s/n, 13071 Ciudad Real, Spain
[b]Cervenka Consulting, Predvoje 22, 16 00 Prague, Czech Republic
[c]ETS Ingenieros de Caminos, Universidad Politécnica de Madrid, Ciudad Universitaria, 28040 Madrid, Spain
[d]Department of Civil Environmental and Architectural Engineering, University of Colorado, Boulder, CO 80309-0428, USA

Received 7 July 2000; accepted 16 April 2002

Abstract

This paper presents a numerical procedure for mixed mode fracture of quasi-brittle materials. The numerical procedure is based on the cohesive crack approach and extends it to mixed mode fracture. The crack path is obtained, and the mixed mode fracture model is incorporated into the crack path. The crack model is based on the formulation of the classical plasticity. The model is incorporated into a commercial finite element code by an user subroutine and is contrasted with experimental results. The numerical results agree quite well with two experimental sets of mixed mode fracture of concrete beams; one from Arrea and Ingraffea, the other from a nonproportional loading by the authors. Two other sets of experimental fracture results were modeled based on double-edge notched testing. The numerical procedure, mainly based on standard properties of the material measured by standard methods, predicts the experimental records of the load versus displacement at several control points of the specimens for three homothetic sizes of specimen.

Keywords: Crack detection; Finite element analysis; Mechanical properties; Mixed mode fracture

1. Introduction

Considerable effort has been devoted in recent years to developing numerical models to simulate the fracture behaviour of quasi-brittle materials, such as mortar, concrete, rock or bricks used in civil engineering structures. Traditionally, the numerical methods based on the finite element method (FEM) are classified into two groups [1]: "smeared crack approach" and "discrete crack approach"; although some authors include a third group: the "lattice approach" [2].

In the smeared crack approach the fracture is represented in a smeared manner: An infinite number of parallel cracks of infinitely small opening are (theoretically) distributed (smeared) over the finite element [3]. The cracks are usually modelled on a fixed finite element mesh. Their propagation is simulated by the reduction of the stiffness and strength of the material. The constitutive laws, defined by stress–strain relations, are nonlinear and show a *strain softening*. This approach was pioneered with fixed crack orthotropic secant models [4–6] and rotating crack models [7–9]. More elaborarate models have also been proposed [10,11].

However, strain softening introduces some difficulties in the analysis. The system of equations may become ill-posed [12–14], localization instabilities and spurious mesh sensivity of finite element calculations may appear [3]. These difficulties can be tackled by supplementing the material model with some mathematical condition [15–17]. Other strategies are the nonlocal continuum models [18,19], the gradient models [20] and the micropolar continuum [21]. These procedures are suited to specific problems, but none gives a general solution of the problem.

The discrete approach is preferred when there is one crack, or a finite number of cracks, in the structure. The cohesive crack model, developed by Hillerborg et al. [22]

Abbreviations: ASTM, American Society for Testing and Materials; CEB, Comité Euro-International du Béton; CMOD, crack mouth opening displacement; CMSD, crack mouth sliding displacement; FEM, finite element method; GBF, general bilinear fit; LEFM, linear elastic fracture mechanics; MTS, maximum tangential stress; RILEM, Réunion Internationale des Laboratoires d'Essais et de Recherches sur les Matériaux et les Constructions.

* Corresponding author.
E-mail addresses: jgalvez@ccp-cr.uclm.es (J.C. Gálvez), cervenka@cervenka.cz (J. Červenka), david@mater.upm.es (D.A. Cendón), saouma@civil.colorado.edu (V. Saouma).

0008-8846/02/$ – see front matter © 2002 Elsevier Science Ltd. All rights reserved.
PII: S0008-8846(02)00825-6

for Mode I fracture of concrete, was shown to be efficient to model the fracture process of quasi-brittle materials. It has been extended to mixed mode fracture (Modes I and II) and incorporated into finite element codes [23–27] and to boundary element codes [28]. One of the difficulties associated with these codes is that they require an input of material properties that are difficult to evaluate. In the absence of experimental data, these properties are estimated, but no systematic research has clarified their influence on mixed mode fracture. The authors usually fit these properties to simulate the experimental results. The problem is increased by the wide scatter of the published experimental data on mixed mode fracture; large changes in the material properties allow the numerical predictions to cover this wide experimental scatter. This aspect is especially marked in the crack paths. Gálvez et al. [30] developed a set of mixed mode fracture tests of concrete beams under proportional and nonproportional loading, which gave different families of crack paths in three sizes of specimens. The experimental scatter of these tests was very narrow, and they are one of the references, complementary to others, for mixed mode fracture models, since the model should predict the crack path and the experimental records of load versus displacement at several control points of the specimens, all for three specimen sizes and two mixed mode loading conditions.

This work presents a procedure that reproduces the fracture proccess of the quasi-brittle materials under mixed loading using the discrete crack approach. It predicts the crack path and the mechanical behaviour of the specimen as the crack grows. The cohesive model is largely based on the model of Červenka [23], which was successful in the analysis of bimaterial interfaces [29] with a special purpose finite element code [24]. The formulation of the model is based on the formulation of classical plasticity. The model is complementary to other models having the advantage that only includes parameters with physical meaning and experimentally measurable.

It is shown [30,31], for quasi-brittle materials, that under a *global* mixed mode loading, the crack grows with a predominantly *local* Mode I fracture. This important point allows a formulation of mixed mode fracture models mainly based on standard properties of the material, measured by standardized methods: tensile strength, compression strength, Young's modulus and Mode I specific fracture energy. Other parameters not measurable by standard methods, such as Mode II specific fracture energy, may be brought into its varying range with little influence on the final result, as it is shown in this paper. This allows an important change in the formulation of mixed mode fracture models. The models may be calibrated by standard tests before the mixed mode tests, and, in fact, they *predict* the experimental results of the mixed mode fracture tests and may be termed *predictive models*. Until now, in general terms, the models were calibrated by mixed mode tests, then 'predicting' the experimental results of mixed mode fracture tests, becoming *postdictive models* instead.

The model has been incorporated into a commercial multipurpose finite element code by an user subroutine and experimentally contrasted. Numerical results agree quite well with two experimental sets of mixed mode fracture of concrete beams: one of Gálvez et al. and one of Arrea and Ingraffea. Numerical simulations with different values of Mode II parameters were developed, with little influence on the numerical predictions. Two other sets of experimental fracture results, based on the double-edge notched testing procedure, were modeled, also with a good fit. In all cases, the model was calibrated before the mixed mode tests, mainly on the basis of the standard properties of the material, and it predicted the experimental records of the load versus displacement at several control points of the specimens for three specimen sizes.

2. The cohesive crack model in Mode I

The cohesive crack model, called *fictitious crack model* by Hillerborg et al. [22], has been successful in the analysis of the fracture of concrete, rock and cement based materials since its proposal, as shown in Refs. [37,38] among other researches in this field. Part of this success is due to its simplicity and physical meaning. A detailed review of this model was done in Ref. [3]. The softening function, $\sigma = f(w)$, is the main ingredient of the cohesive crack model. This function, a material property, relates the stress σ acting across the crack faces to the corresponding crack opening w (see Fig. 1). In Mode I opening, the stress transferred, σ, is normal to the crack faces.

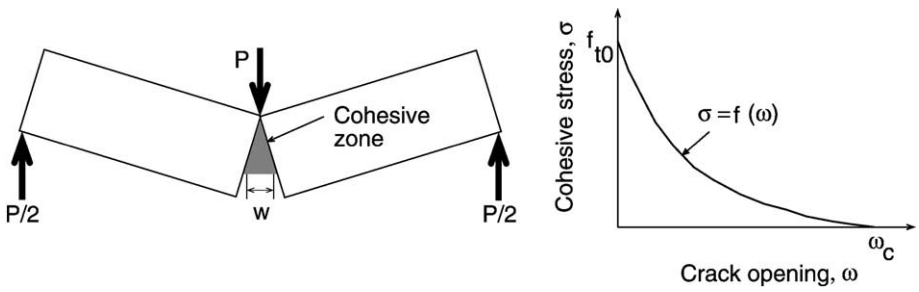

Fig. 1. Cohesive crack and softening curve for Mode I fracture of concrete.

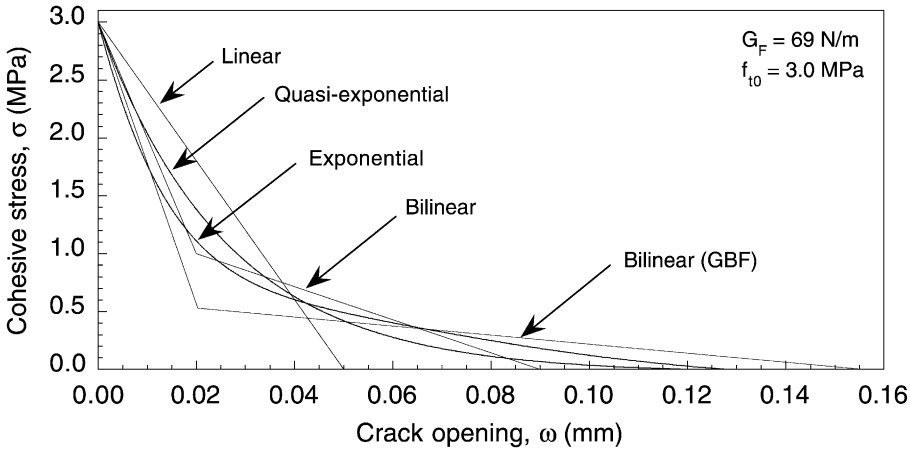

Fig. 2. Softening curves for concrete.

Two properties of the softening curve are most important: the tensile strength, f_{t_0}, and the cohesive fracture energy, G_F. The tensile strength is the stress at which the crack is created and starts to open ($f(0)=f_{t_0}$). The cohesive fracture energy, G_F, also called *specific fracture energy*, is the external energy required to create and fully break a unit surface area of a cohesive crack and coincides with the area under the softening function. The tensile strength and the specific fracture energy are material properties and may be experimentally measured in accordance with American Society for Testing and Materials (ASTM) C 496 [39] and Réunion Internationale des Laboratoires d'Essais et de Recherches sur les Matériaux et les Constructions (RILEM) 50-FMC [40], respectively.

Many softening curves have been developed to model the experimental fracture behaviour of concrete in tension [3]. The bilinear curves are accepted as reasonable approximations of the softening curve for concrete (Fig. 2), although there is no agreement about the precise location of the kink point. Smoother curves have also been proposed: exponential [41–43] and power law [44], among others.

3. The cohesive crack model in mixed mode

The numerical simulation of the mixed mode (I/II) fracture process of concrete is based on the incorporation of the cohesive crack model into a finite element code. The two main stages of the process are the calculation of the crack path and the incorporation of the cohesive crack model into the crack path; these stages are two different computational steps.

3.1. Numerical prediction of the crack path

Linear elastic fracture mechanics (LEFM) has proven its worth to predict the crack path, even for complex trajectories [30,31]. In this work, numerical computations use the maximum tangential stress (MTS) criterion [45], which postulates that the crack grows in the direction perpendicular to that of the greatest tension. Detailed information about the MTS criterion can be found in Ref. [46], for example. The LEFM finite element code FRANC2D [47] was used to calculate the crack paths.

The assumption of this criterion in mixed mode fracture implies that the crack grows in a stable manner in local Mode I under global mixed mode loading. There is an important local mixed mode when the crack starts from the notch. This is shown by a kink between the notch and the crack. A finite element calculation of K_I and K_{II} at the tip of the notch shows this local mixed mode. When the crack is growing in a stable manner under mixed loading, a local Mode I crack growth may be assumed, as is shown by finite element calculations: K_{II} is very small in comparison with K_I. This was shown as valid in stable tests with brittle materials [48,49] and extended to quasi-brittle materials [30,31]. Further testing is needed before it can be used for unstable crack growth.

3.2. Cracking surface for mixed mode fracture

Quasibrittle materials such as rock and concrete do not exhaust the traction strength after a stress equal to the traction strength. Fig. 3 shows a crack growing in these materials. From left to right, we distinguish three zones: (1) the true crack, with no stress transmission through the interface, (2) the *fracture process zone*, where the material has been loaded up to the strength and is partially broken, but with unbroken material bridges, and is able to transmit stresses through the interface and (3) the intact material, where the material has not been loaded up to the strength. The cohesive crack model for Mode I reproduces this behaviour by the softening curve for the normal strength crack, σ, as shown Fig. 1.

In mixed mode (I and II) fracture, the interaction between normal stress, σ, and tangential stress, τ, should be taken into account. It is assumed that the crack grows when the combination of normal stress, σ, and the tangential stress, τ, reaches a cracking surface $F(\sigma,\tau)=0$, like a yield surface in

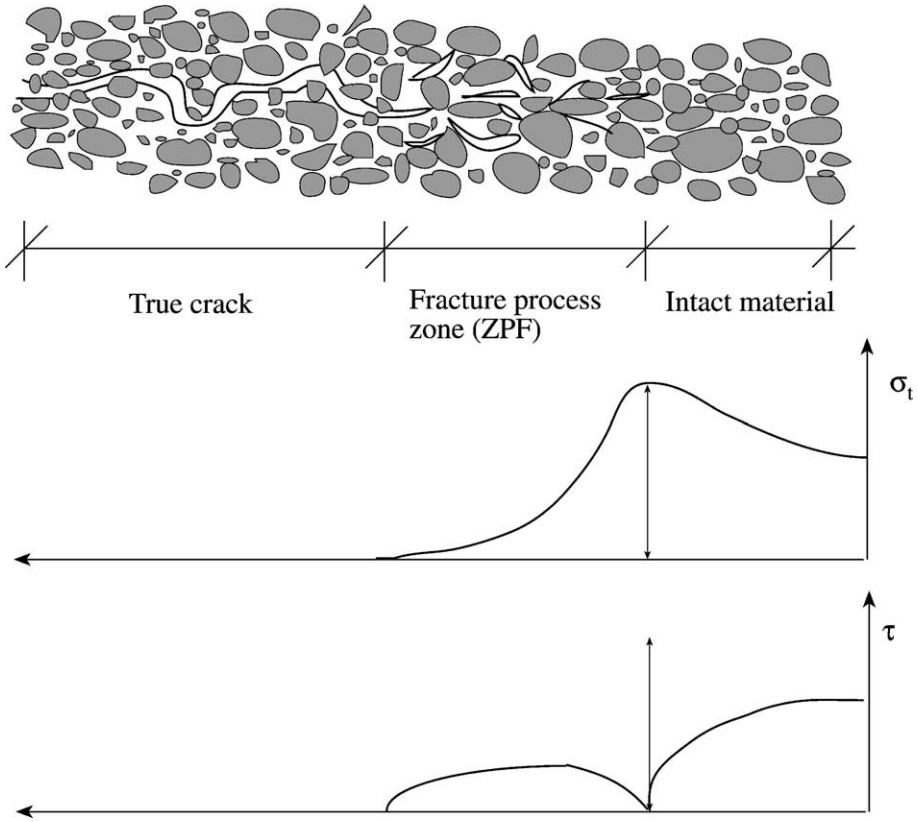

Fig. 3. Cracking process in concrete and profiles of traction and tangential stresses.

classical plasticity. This work assumes the following hyperbolic expression [14]:

$$F = \tau^2 - 2c\tan\phi_f(f_t - \sigma) - \tan^2\phi_f(\sigma^2 - f_t^2) \quad (1)$$

where c is the cohesion, ϕ_f the friction angle, and f_t the tensile strength.

In accordance with the cohesive approach [22], the cracking surface evolves with the opening of the crack, following the softening curves of the tensile strength, f_t, and the cohesion, c.

The *traction vector*, $\boldsymbol{t}$, is defined from the normal stress, σ, and the stress, τ, tangential to the crack faces (Eq. (2)):

$$\boldsymbol{t} = \sigma\vec{n} + \tau\vec{t} \quad (2)$$

where $\vec{n}$ and $\vec{t}$ are the unit vectors in the normal and tangential directions to the crack faces.

The incremental inelastic displacement vector between the crack faces, $\dot{\boldsymbol{u}}^i$, is defined. This vector is obtained from

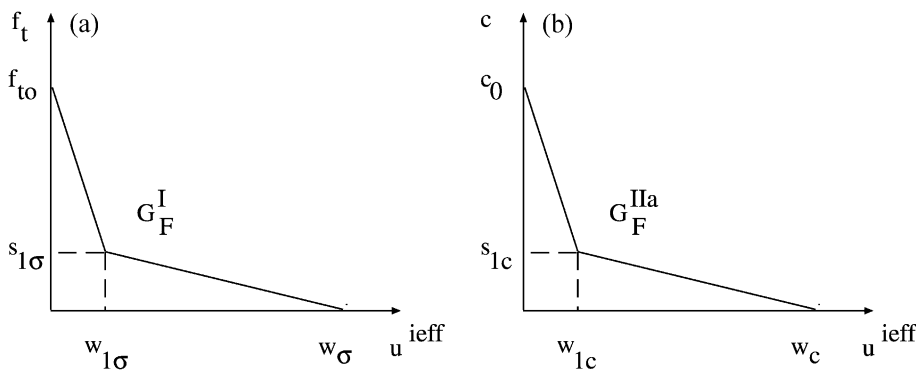

Fig. 4. Softening curves: (a) traction strength, σ; (b) cohesion, c.

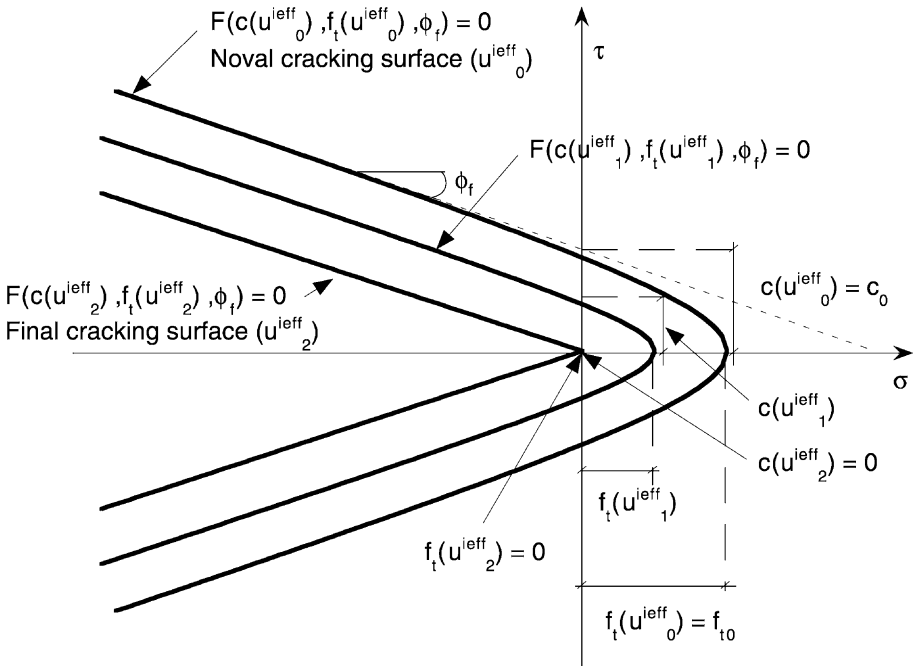

Fig. 5. Cracking surface and evolution.

the normal, $\dot{u}^{\mathrm{i}}_{\mathrm{n}}$, and the tangential, $\dot{u}^{\mathrm{i}}_{\mathrm{t}}$, to the crack faces incremental relative inelastic displacements (Eq. (3)):

$$\dot{\boldsymbol{u}}^{\mathrm{i}} = \dot{u}^{\mathrm{i}}_{\mathrm{n}}\vec{n} + \dot{u}^{\mathrm{i}}_{\mathrm{t}}\vec{t} \tag{3}$$

The $\dot{\boldsymbol{u}}^{\mathrm{i}}$ vector is obtained by the decomposition of the incremental relative displacement vector between the crack faces, $\dot{\boldsymbol{u}}$, in an elastic part, $\dot{\boldsymbol{u}}^{\mathrm{e}}$, and an inelastic part, $\dot{\boldsymbol{u}}^{\mathrm{i}}$. The softening parameter, u^{ieff}, is the integral of the modulus of the incremental inelastic displacements along the fracture process. The incremental traction vector, $\dot{\boldsymbol{t}}$, is obtained from the incremental elastic displacements, $\dot{\boldsymbol{u}}^{\mathrm{e}}$. This is expressed as follows (Eqs. (4)–(7)):

$$\dot{\boldsymbol{u}} = \dot{\boldsymbol{u}}^{\mathrm{e}} + \dot{\boldsymbol{u}}^{\mathrm{i}} \tag{4}$$

$$\dot{\boldsymbol{t}} = \boldsymbol{E}\dot{\boldsymbol{u}}^{\mathrm{e}} \tag{5}$$

$$\dot{u}^{\mathrm{ieff}} = \| \dot{\boldsymbol{u}}^{\mathrm{i}} \| = \left(\dot{u}^{i^2}_{\mathrm{n}} + \dot{u}^{i^2}_{\mathrm{t}}\right)^{\frac{1}{2}} \tag{6}$$

$$u^{\mathrm{ieff}} = \int \dot{u}^{\mathrm{ieff}}\,\mathrm{d}t \tag{7}$$

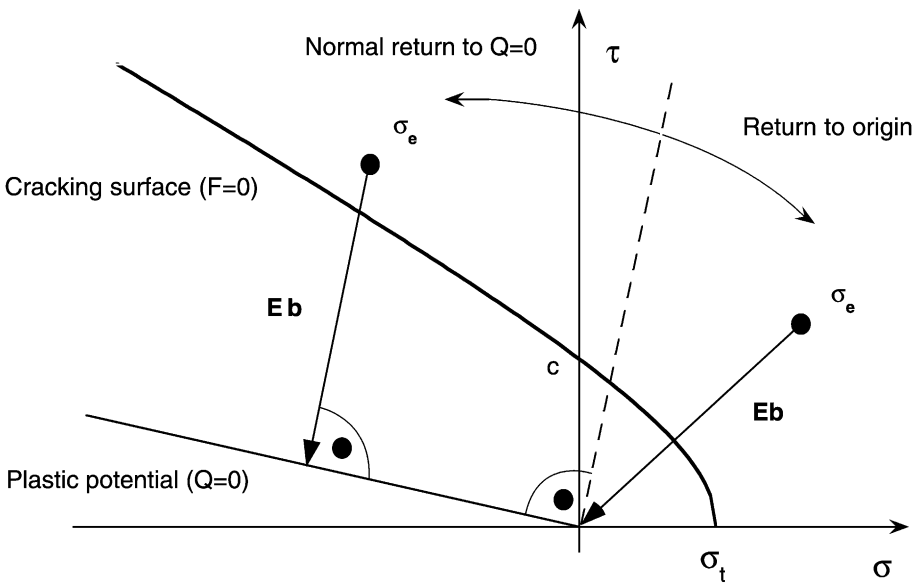

Fig. 6. Return direction to the cracking surface of the inelastic corrector.

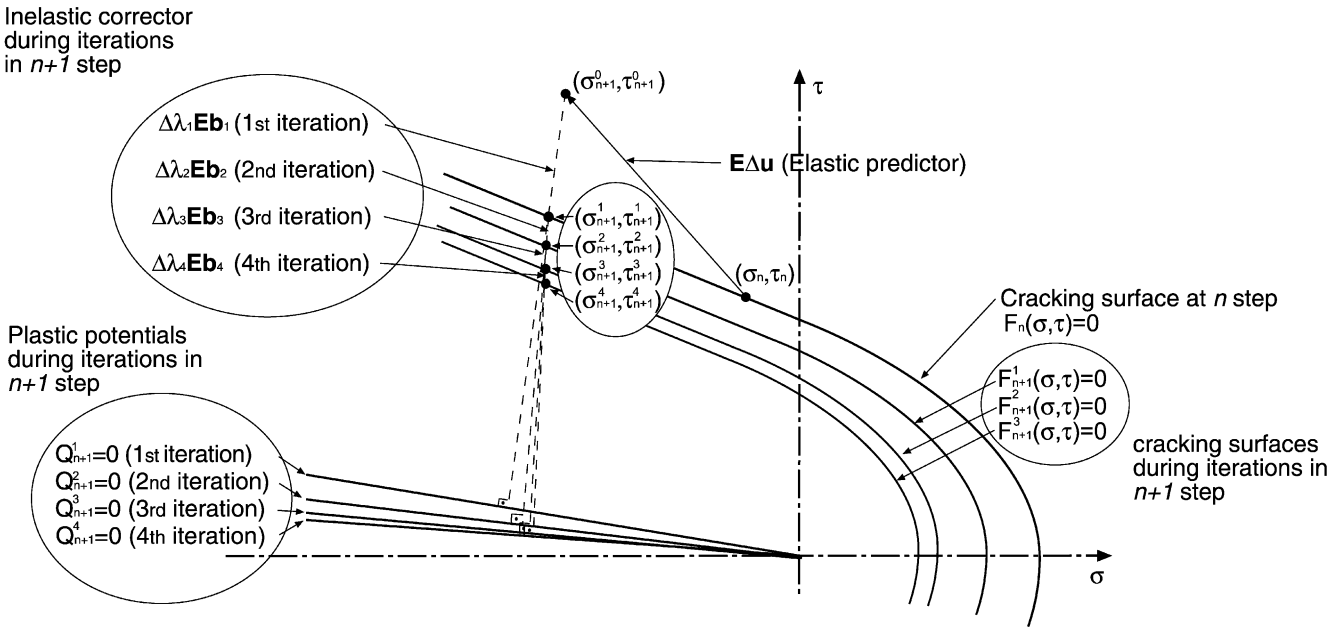

Fig. 7. Graphic interpretation of the iterative process of the cracking surface definition and the placing over it, based on the u^{ieff} parameter evolution.

where $\boldsymbol{E}$ is the elastic tensor and $\dot{u}_n^i$ and $\dot{u}_t^i$ are the normal and tangential incremental relative displacements to the crack faces.

In this way, the traction strength and the cohesion are expressed as functions of the softening parameter, u^{ieff}: $f_t = f_t(u^{ieff})$ and $c = c(u^{ieff})$. Bilinear softening curves were adopted in this work, as Fig. 4 shows. In these curves, G_F^I and G_F^{IIa} are the specific fracture energy in Mode I and Mode IIa (Mode II with a large normal confinement); $s_{1\sigma}$, $\omega_{1\sigma}$, s_{1c} and ω_{1c} are the coordinates of the kink points. It is assumed that the friction angle, ϕ_f, is constant throughout the fracture process.

Fig. 5 shows the cracking surface and its evolution for several cracking conditions, based on the u^{ieff} parameter value. Under pure Mode I ($\tau = 0$), Eq. (1) is expressed as follows (Eq. (8)):

$$F = 2c\tan\phi_f(f_t - \sigma) + \tan^2\phi_f(\sigma^2 - f_t^2) = (f_t - \sigma)\{2c\tan\phi_f - \tan^2\phi_f(f_t + \sigma)\} = 0 \quad (8)$$

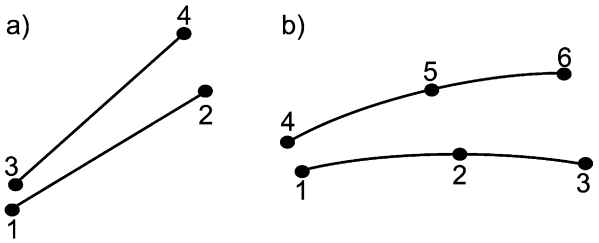

Fig. 8. Interface elements: (a) linear; (b) quadratic.

adopting the solution with physical meaning (Eq. (9)):

$$f_t - \sigma = 0 \quad (9)$$

the expression developed by Hillerborg et al. [22].

It is worth noting that under high damage of the crack, $f_t = 0$ and $c = 0$, the cracking surface evolves to a Coulomb friction surface, with friction coefficient $\mu = \tan\phi_f$, as shown in Fig. 5.

3.3. Dilatancy

The model is incomplete until the evolution of the inelastic displacements in the fracture process zone is

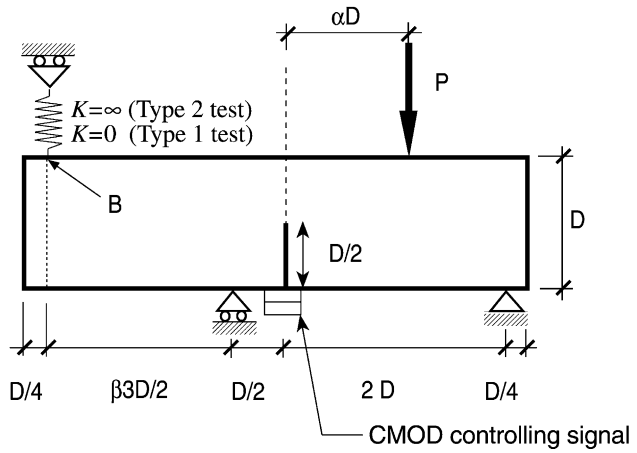

Fig. 9. Geometry, forces and boundary conditions of the tests of Gálvez et al. [30].

Table 1
Dimensions of the prismatic specimens and number of tests by Gálvez et al. [30]

Specimen type	Depth (mm)	Length (mm)	Eccentricity factors		Number of tests	
			α	β	Type 1	Type 2
D1	75	340	1.133	1	6	4
D2	150	675	1	1	6	6
D3	300	1350	1	0.89	4	5

Thickness: 50 mm.

defined. In cohesive–frictional materials such as concrete or mortar, the tangential tractions in a crack generate crack slip, and at the same time lead to a crack opening caused by the irregularities along the crack plane. This effect is named *dilatancy*. The dilatancy fixes the incremental normal and tangential displacement ratio (Eq. (10)):

$$\tan\phi_{\mathrm{d}} = \frac{\dot{u}_{\mathrm{n}}^{\mathrm{i}}}{\dot{u}_{\mathrm{t}}^{\mathrm{i}}} \tag{10}$$

In classical plasticity, the expression of the direction of the inelastic deformations is known as *flow rule* and is normal to the plastic potential (Q = cte). In the cohesive–frictional materials, the flow direction is not usually normal to the cracking surface. The directions normal to the cracking surface and to the plastic potential are different, and the plastic formulation is known as *nonassociative plasticity*. The flow rule is expressed as follows (Eq. (11)):

$$\dot{\epsilon}_{ij}^{\mathrm{p}} = \dot{\lambda}\frac{\partial Q}{\partial \sigma_{ij}} \tag{11}$$

where $\dot{\epsilon}_{ij}^{\mathrm{p}}$ is the plastic incremental deformation, $\dot{\lambda}$ is a positive real constant known as the plastic strain-rate multiplier, Q is the plastic potential and σ_{ij} is the ij component of the stress tensor. In this work, the analogous expression, based on the incremental displacement vector, is assumed (Eq. (12)):

$$\dot{\boldsymbol{u}}^{\mathrm{i}} = \dot{\lambda}\frac{\partial Q(\boldsymbol{t})}{\partial \boldsymbol{t}} = \dot{\lambda}\boldsymbol{b} \tag{12}$$

where $\dot{\boldsymbol{u}}^{\mathrm{i}}$ is the incremental inelastic displacement vector and $\boldsymbol{b}$ is the direction vector normal to the plastic potential, which is the return direction to the cracking surface. The angle between the plastic potential, Q = cte, and the abscissa in the traction region is the *dilatancy angle*, ϕ_{d}. The ϕ_{d} evolution is also defined from the softening parameter, u^{ieff}, diminishing as the opening crack grows. Following Ref. [23], a linear curve has been adopted:

$$\phi_{\mathrm{d}} = \begin{cases} \phi_{\mathrm{d,max}}\left(1 - \frac{u^{\mathrm{ieff}}}{u_{\mathrm{cri,dil}}}\right) & \forall u^{\mathrm{ieff}} < u_{\mathrm{cri,dil}} \\ 0 & \forall u^{\mathrm{ieff}} > u_{\mathrm{cri,dil}} \end{cases}$$

where $\phi_{\mathrm{d,max}}$ is the initial value of the dilatancy angle, and $u_{\mathrm{cri,dil}}$ is the critical relative displacement after which the interface ceases to exhibit the dilatancy effect.

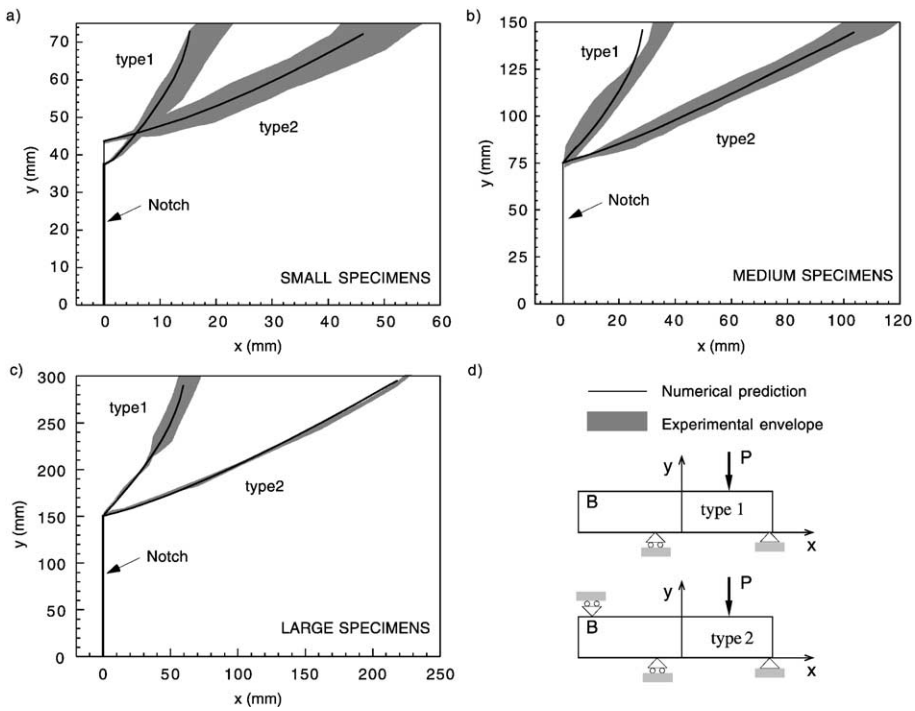

Fig. 10. Experimental envelopes and numerical predictions of the crack paths in the tests of Gálvez et al. [30]: (a) small specimens (D = 75 mm); (b) medium specimens (D = 150 mm); (c) large specimens (D = 300 mm); and (d) legend and axes of reference.

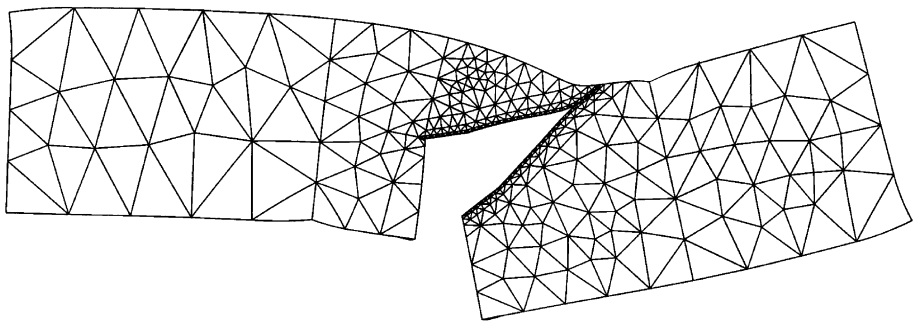

Fig. 11. Deformed finite element mesh of the medium size ($D = 150$ mm) Type 2 tests of Gálvez et al. [30].

When the traction stress, σ, is predominant over the tangential stress, τ, the direction normal to the plastic potential ($Q = \text{cte}$) is not defined. In this case, the return direction to the origin of stresses, $\sigma = 0$ and $\tau = 0$, is adopted, which divides the stress space into two parts. This is graphically shown in Fig. 6.

The displacement from a point of the cracking surface in the stress space is expressed as follows:

$$\dot{\boldsymbol{t}} = \boldsymbol{E}\dot{\boldsymbol{u}}^{e} = \boldsymbol{E}(\dot{\boldsymbol{u}} - \dot{\lambda}\boldsymbol{b}) \tag{13}$$

where $\boldsymbol{E}$ is the elastic tensor, $\boldsymbol{E}\dot{\boldsymbol{u}}$ is the stresses predictor and $\boldsymbol{E}\dot{\lambda}\boldsymbol{b}$ is the inelastic corrector.

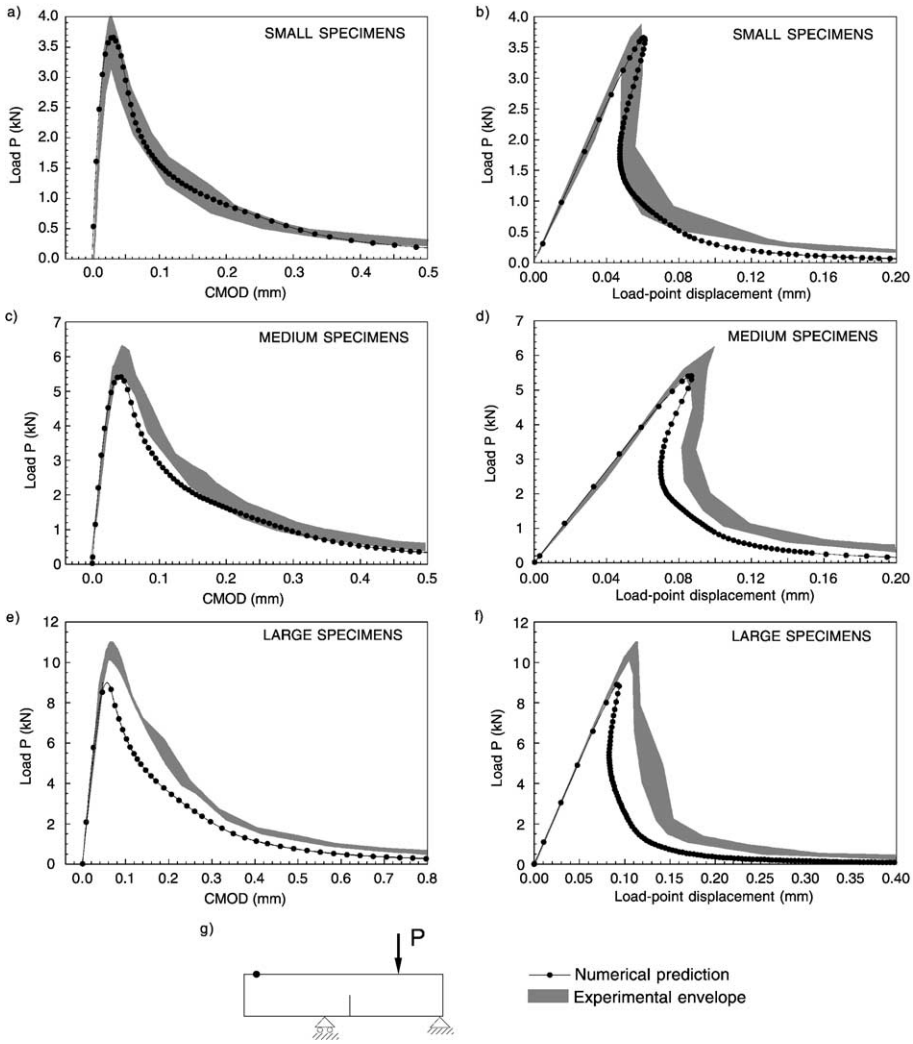

Fig. 12. Experimental envelopes and numerical predictions of the Type 1 tests of Gálvez et al. [30]. Small size ($D = 75$ mm): (a) load–CMOD; (b) load–displacement. Medium size ($D = 150$ mm): (c) load–CMOD; (d) load–displacement. Large size ($D = 300$ mm): (e) load–CMOD; (f) load–displacement. (g) Legend and scheme of the tests.

3.4. Integrating the rate equations

The mathematical theory of plasticity is used in the development of the constitutive driver for the interface crack model. For a given state in the n step, the traction vector, $\boldsymbol{t}_n$, and the softening parameter, u_n^{ieff}, are known. Let us assume that in the n step, the crack is growing, so the cracking surface equation is satisfied: $F(\boldsymbol{t}_n, u_n^{\text{ieff}}) = 0$.

An incremental relative displacement between crack faces is adopted, $\Delta\boldsymbol{u}_n = \boldsymbol{u}_{n+1} - \boldsymbol{u}_n$, and the new traction state, $\boldsymbol{t}_{n+1}$, is calculated as follows (Eq. (14)):

$$\boldsymbol{t}_{\text{e}} = \boldsymbol{t}_n + \boldsymbol{E}\Delta\boldsymbol{u}_n \tag{14}$$

where $\boldsymbol{t}_{\text{e}}$ is a new traction vector, obtained from an *elastic predictor*. If the crack is growing in the $n+1$ state, the cracking surface equation should be satisfied, $F(\boldsymbol{t}_{n+1}, u_{n+1}^{\text{ieff}}) = 0$, and the traction vector, $\boldsymbol{t}_{n+1}$, is obtained from $\boldsymbol{t}_{\text{e}}$, adopting an inelastic corrector (Eq. (15)):

$$t_{n+1} = \boldsymbol{t}_{\text{e}} - \Delta\lambda_n \boldsymbol{E}\boldsymbol{b}_n \tag{15}$$

where $\Delta\lambda_n \boldsymbol{E}\boldsymbol{b}_n$ is the inelastic corrector, $\boldsymbol{E}$ is the elastic tensor and $\boldsymbol{E}\boldsymbol{b}_n$ is the return direction vector to the plastic potential ($Q = \text{cte}$). $\Delta\lambda_n$ is obtained since the cracking surface equation must be satisfied in the $n+1$ state:

$$F(\boldsymbol{t}_{n+1}, u_n^{\text{ieff}}) = F(\boldsymbol{t}_{\text{e}} - \Delta\lambda_n \boldsymbol{E}\boldsymbol{b}_n, u_n^{\text{ieff}}) = 0 \tag{16}$$

which, expressed as a function of traction strength and cohesion, gives Eq. (17):

$$F(\boldsymbol{t}_{n+1}, c_n, f_{\text{t}_n}) = 0 \tag{17}$$

where f_{t_n} and c_n are the traction strength and cohesion at the n state. The parameters involved in the procedure are actualized:

$$\Delta u_n^{\text{ieff}} = ||\Delta \boldsymbol{u}_{\text{n}}^{\text{i}}|| = \Delta\lambda_n ||\boldsymbol{b}_n||$$

$$u_{n+1}^{\text{ieff}} = u_n^{\text{ieff}} + \Delta u_n^{\text{ieff}}$$

$$f_{\text{t}_{n+1}} = f_{\text{t}}(u_{n+1}^{\text{ieff}})$$

$$c_{n+1} = c(u_{n+1}^{\text{ieff}})$$

$$\phi_{\text{d}_{n+1}} = \phi_{\text{d}}(u_{n+1}^{\text{ieff}})$$

$$\boldsymbol{b}_{n+1} = \boldsymbol{b}(u_{n+1}^{\text{ieff}}) \tag{18}$$

It is worth noting that the traction strength, f_{t}, the cohesion, c, the return direction, $\boldsymbol{E}\boldsymbol{b}$, and the dilatancy angle, ϕ_{d}, used in Eq. (16) corresponding to the n state are not actualized to the $n+1$ state. This is so because the value of the softening parameter, u^{ieff}, is obtained once the increment of the plastic multiplier, $\Delta\lambda$, is known. This leads to an iterative process where the new value of u^{ieff} defines a

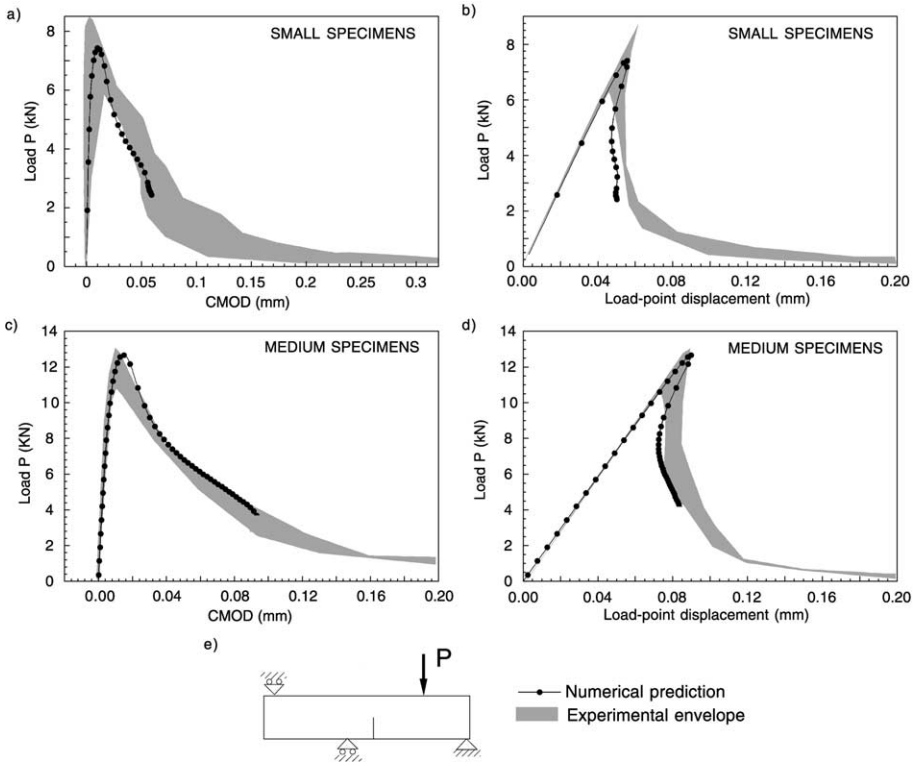

Fig. 13. Experimental envelopes and numerical predictions of the Type 2 tests of Gálvez et al. [30]. Small size ($D = 75$ mm): (a) load–CMOD; (b) load–displacement. Medium size ($D = 150$ mm): (c) load–CMOD; (d) load–displacement. (e) Legend and scheme of the tests.

new cracking surface and a new return direction to it, which gives a new value of $\Delta\lambda$, and this leads to a new value of u^{ieff}. The iteration process ends when the inelastic correction is below a prefixed value, that is to say, the $\Delta\lambda$ value obtained in Eq. (16) is smaller than a fixed ϵ value. Fig. 7 shows graphically the iterative process.

3.5. Incorporation into a finite element code

The above model was incorporated into the finite element code ABAQUS© by means of an user subroutine. Since the Newton–Raphson algorithm solver was used, the tangent stiffness matrix is necessary.

The cracking surface is expressed as a function of the traction vector, $\boldsymbol{t}$, and the softening parameter, u^{ieff}, so its variation may be expressed as follows (Eq. (19)):

$$\mathrm{d}F = \frac{\partial F}{\partial \boldsymbol{t}} \cdot \mathrm{d}\boldsymbol{t} + \frac{\partial F}{\partial u^{\text{ieff}}} \mathrm{d}u^{\text{ieff}} \tag{19}$$

The movement over the cracking surface leads to a null gradient, so:

$$\mathrm{d}F = \frac{\partial F}{\partial \boldsymbol{t}} \cdot \mathrm{d}\boldsymbol{t} + \frac{\partial F}{\partial u^{\text{ieff}}} \mathrm{d}u^{\text{ieff}} = 0 \tag{20}$$

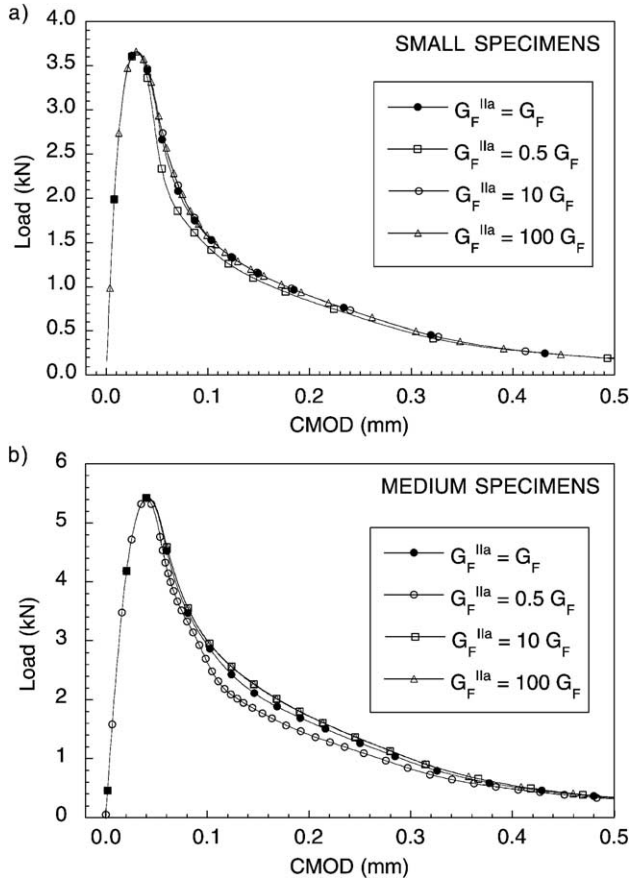

Fig. 14. Numerical predictions of the load–CMOD curves of the Type 1 tests of Gálvez et al. [30] with $G_F^{IIa} = 0.5$, 1.10 and 100 G_F: (a) small size ($D = 75$ mm) and (b) medium size ($D = 150$ mm).

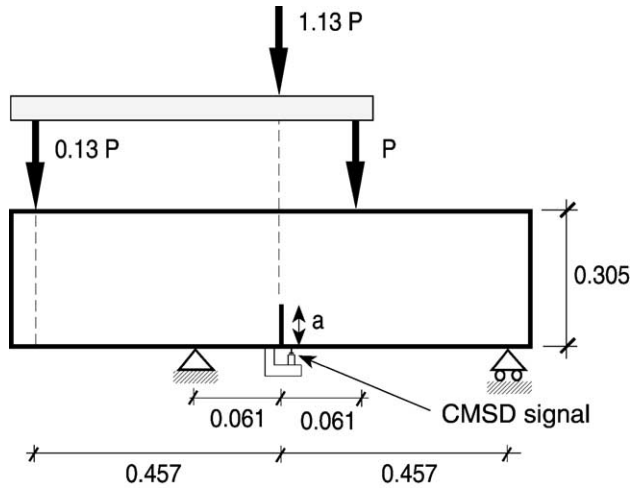

Fig. 15. Geometry, forces and boundary conditions of the tests of Arrea and Ingraffea [32].

and based on the flow definition:

$$\mathrm{d}u^{\text{ieff}} = \mathrm{d}\lambda||\boldsymbol{b}|| \tag{21}$$

From Eq. (13):

$$\mathrm{d}\boldsymbol{t} = \boldsymbol{E}(\mathrm{d}\boldsymbol{u} - \mathrm{d}\lambda\boldsymbol{b}) \tag{22}$$

and substituting Eqs. (21) and (22) in Eq. (20), we have Eq. (23):

$$\mathrm{d}F = \frac{\partial F}{\partial \boldsymbol{t}} \cdot [\boldsymbol{E}(\mathrm{d}\boldsymbol{u} - \mathrm{d}\lambda\boldsymbol{b})] + \frac{\partial F}{\partial u^{\text{ieff}}} \mathrm{d}\lambda||\boldsymbol{b}|| = 0 \tag{23}$$

This leads to finding $\mathrm{d}\lambda$ (Eq. (24)):

$$\mathrm{d}\lambda = \frac{\frac{\partial F}{\partial \boldsymbol{t}} \cdot \boldsymbol{E}\mathrm{d}\boldsymbol{u}}{\frac{\partial F}{\partial \boldsymbol{t}} \cdot \boldsymbol{E}\boldsymbol{b} - \frac{\partial F}{\partial u^{\text{ieff}}}||\boldsymbol{b}||} \tag{24}$$

and replacing this value in Eq. (22) yields:

$$\mathrm{d}\boldsymbol{t} = \left(\boldsymbol{E} - \frac{\boldsymbol{E}\boldsymbol{b} \otimes \boldsymbol{E}^{\mathrm{T}} \frac{\partial F}{\partial \boldsymbol{t}}}{\frac{\partial F}{\partial \boldsymbol{t}} \cdot \boldsymbol{E}\boldsymbol{b} - \frac{\partial F}{\partial u^{\text{ieff}}}||\boldsymbol{b}||}\right) \mathrm{d}\boldsymbol{u} \tag{25}$$

the tangent tensor is obtained:

$$\mathrm{d}\boldsymbol{t} = \boldsymbol{C}^{\text{ep}}\mathrm{d}\boldsymbol{u} \Rightarrow \boldsymbol{C}^{\text{ep}} = \boldsymbol{E} - \frac{\boldsymbol{E}\boldsymbol{b} \otimes \boldsymbol{E}^{\mathrm{T}} \frac{\partial F}{\partial \boldsymbol{t}}}{\frac{\partial F}{\partial \boldsymbol{t}} \cdot \boldsymbol{E}\boldsymbol{b} - \frac{\partial F}{\partial u^{\text{ieff}}}||\boldsymbol{b}||} \tag{26}$$

and as $\boldsymbol{b} = \partial Q/\partial \boldsymbol{t}$, we name $\boldsymbol{a} = \partial F/\partial \boldsymbol{t}$, compacting Eq. (26) to:

$$\boldsymbol{C}^{\text{ep}} = \boldsymbol{E} - \frac{\boldsymbol{E}(\boldsymbol{b} \otimes \boldsymbol{a})\boldsymbol{E}}{\boldsymbol{a} \cdot \boldsymbol{E}\boldsymbol{b} - \frac{\partial F}{\partial u^{\text{ieff}}}||\boldsymbol{b}||} \tag{27}$$

Table 2
Material properties of the tests of Arrea and Ingraffea [32]

Series	f_c[a] (Mpa)	E[a] (GPa)	ν[a]	f_{t_0}[b] (MPa)	G_F[b] (N/m)
A	60.7	23.4	0.21	4.6	75
B	45.5	24.8	0.18	3.7	107
C	43.4	24.8	0.18	3.4	110

[a] From Arrea and Ingraffea [32].
[b] From CEB-FIP [52].

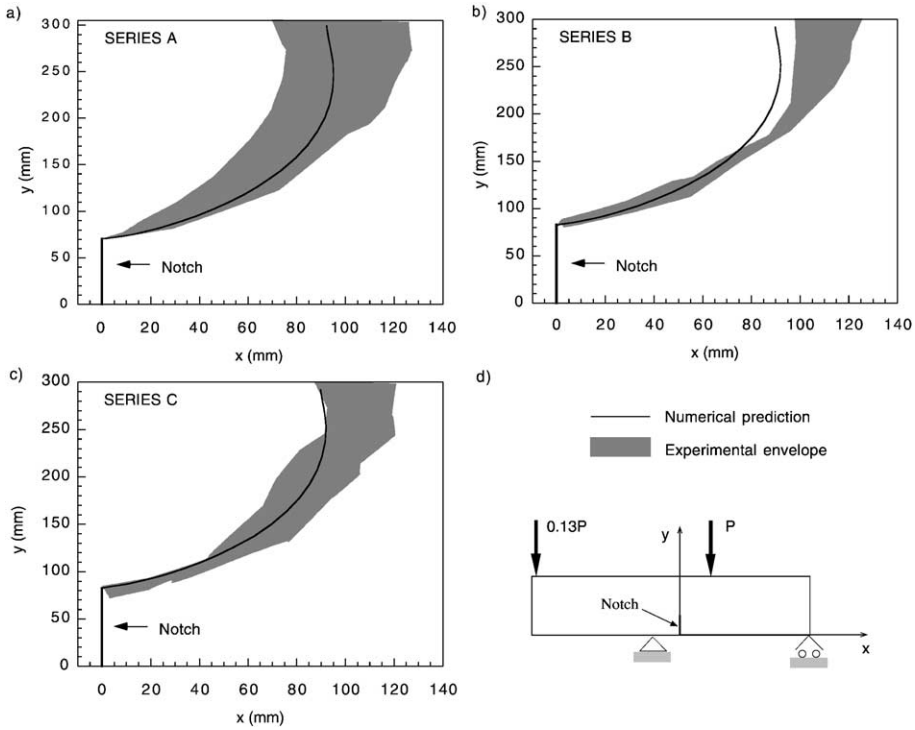

Fig. 16. Experimental envelopes and numerical predictions of the crack trajectories in mixed mode tests of Arrea and Ingraffea [32]: (a) Series A; (b) Series B; (c) Series C; and (d) legend and axes of reference.

The tangent tensor is seen to be nonsymmetric, except for $\boldsymbol{a}=\boldsymbol{b}$, which is the associative plasticity case.

The only unknown value is $\partial F/\partial u^{\mathrm{ieff}}$, which is obtained by means of the chain rule (Eq. (28)):

$$\frac{\partial F}{\partial u^{\mathrm{ieff}}}=\frac{\partial F}{\partial c}\frac{\partial c}{\partial u^{\mathrm{ieff}}}+\frac{\partial F}{\partial f_{\mathrm{t}}}\frac{\partial f_{\mathrm{t}}}{\partial u^{\mathrm{ieff}}} \tag{28}$$

where f_{t} is the traction strength and c is the cohesion for the actualized value of u^{ieff}.

Two interface elements were developed to incorporate the model into the ABAQUS code. The formulation is based on the virtual works theorem. Appendix A gives details of the element formulation. Fig. 8 is a sketch of the interface elements: linear and quadratic.

4. Analysis of mixed mode loading tests

The numerical procedure is compared with experimental results on mixed mode fracture, using two types of test: (1) mixed mode fracture tests on notched beams, developed by Gálvez et al. [30] and Arrea and Ingraffea [32] and (2)

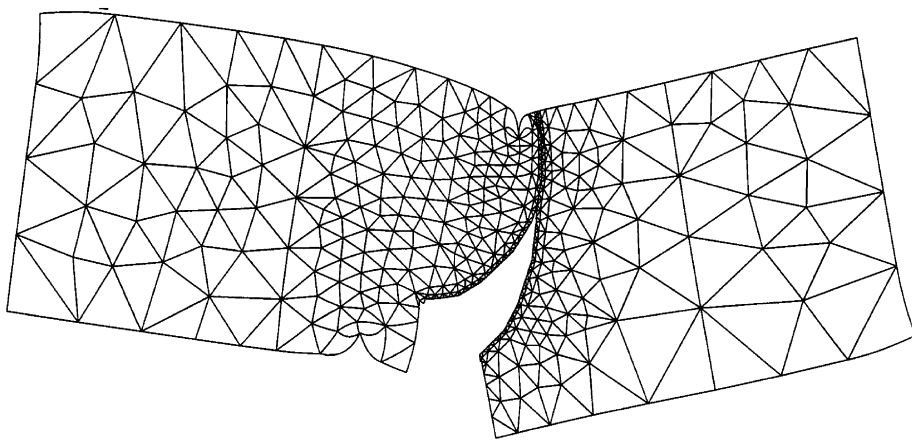

Fig. 17. Deformed finite element mesh of the Series B tests of Arrea and Ingraffea [32].

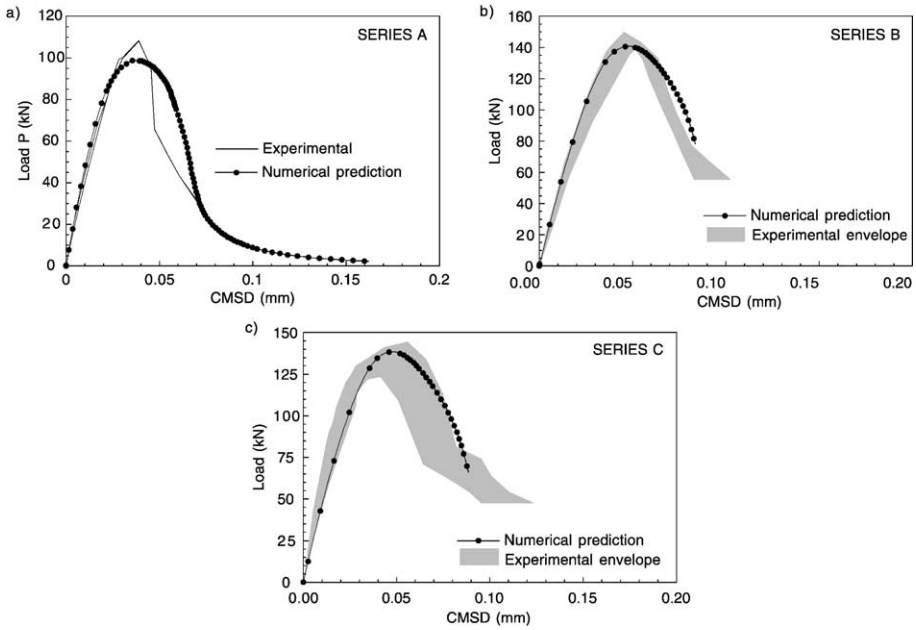

Fig. 18. Experimental envelopes and numerical predictions of the tests of Arrea and Ingraffea [32]. Load P–CMSD curves: (a) Series A; (b) Series B; and (c) Series C.

mixed mode fracture tests on double-edge notched specimens, developed by Reinhardt and Xu [33], Cedolin et al. [35] and Gálvez et al. [36].

4.1. Mixed mode fracture tests on notched beams

4.1.1. Comparison with the experiments by Gálvez

Experimental data on mixed mode fracture of concrete were published recently [30,31]. Two sets of the testing procedure were developed under proportional and nonproportional loading for two different families of crack paths. Three sizes of quasi-homothetic beams were tested. Fig. 9 shows the geometry, forces and boundary conditions of the tests. Table 1 gives the dimensions and number of the specimens for both types of tests. Fracture energy, tensile strength, compressive strength and Young's modulus were measured according to RILEM 50-FMC [40], ASTM C 496 [39], ASTM C 39 [50] and ASTM C 469 [51]. Their values were: $G_F = 69$ N/m, $f_{t_0} = 3.0$ MPa, $f_c = 57$ MPa and $E = 38$ GPa. In accordance with Ref. [23], complementary parameters for the model were estimated: $c = 5.0$ MPa, $\phi_f = 50°$, $\phi_d = 50°$ and $G_F^{IIa} = 69$ N/m.

Fig. 10a–c shows the experimental envelope and the numerical prediction of the crack paths for the two types of test and the three specimen sizes. The numerical prediction

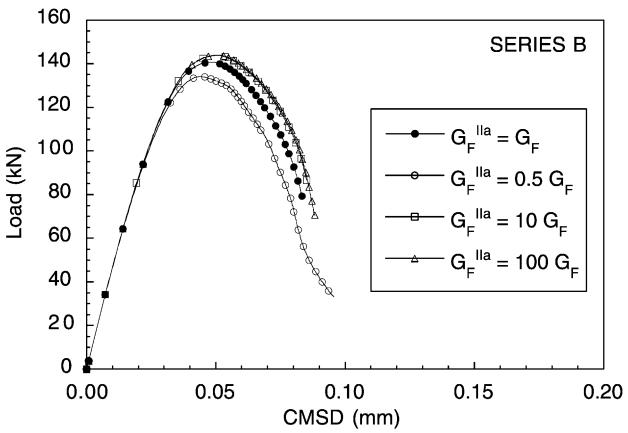

Fig. 19. Numerical predictions of the load–CMSD curves of the Series B tests of Arrea and Ingraffea [32] with $G_F^{IIa} = 0.5$, 1, 10 and 100 G_F.

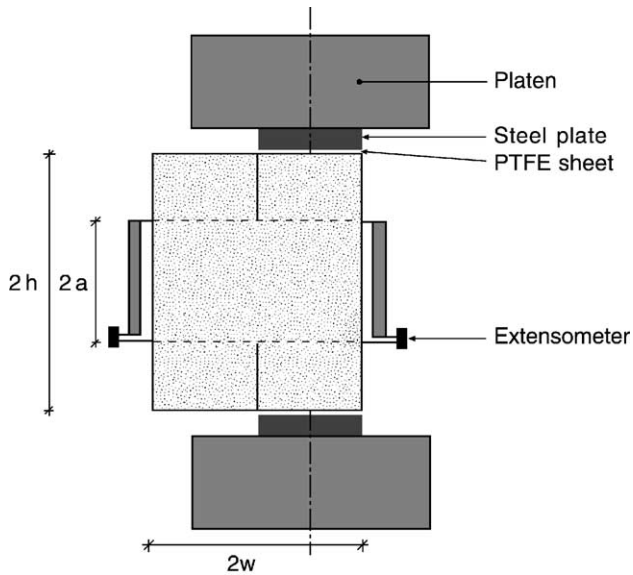

Fig. 20. Geometry and testing arrangement of the tests of Gálvez et al. [36].

Table 3
Dimensions of the specimens and number of tests by Gálvez et al. [36]

Specimen	Height, $2h$ (mm)	Length, $2w$ (mm)	Ligament, $2a$ (mm)	Number of specimens
H75	75	56.25	37.5	3
H150	150	112.5	75	3
H300	300	225	150	3

Thickness: 50 mm.

is a good approximation to the crack path in the narrow experimental scatter band. The accuracy of the prediction lends further support to the hypothesis that the elastic crack path is a good approximation for concrete structures.

Fig. 11 shows a deformed mesh used to study the mixed mode fracture behaviour of the medium size ($D=150$ mm) specimens under nonproportional loading (Type 2 test).

Fig. 12 shows the experimental envelope of Type 1 tests ($K=0$) and the numerical prediction of load P–crack mouth opening displacement (CMOD), and load P versus displacement of the application point of load P, for the three sizes. The numerical model is a good prediction of the experimental results, especially the load P–CMOD curves. In load P versus displacement of the application point of the P, the model predicts the snap-back of the curve. The numerical procedure adequately converges until the end of the curves, to practically null load P.

For Type 2 tests ($K=\infty$), Fig. 13 shows the experimental envelope and the numerical prediction of load P versus displacement of the application point of load P, and load P–CMOD. The numerical model is consistent with the experimental results, especially the load P–CMOD curves and load P versus displacement of the application point of load P. The model predicts the snap-back. The numerical convergence is less close than in the Type 1 tests.

It is worth noting that numerical prediction is based on the material properties measured by standard tests, which are different from the mixed mode fracture tests presented above. On the basis of this set of standard properties, the numerical procedure adequately reproduces the mixed mode P–CMOD and P–displacement experimental records of two types of test and three sizes of specimen.

Large changes in cohesion value, when they lead to a hyperbolic Eq. (1) with physical meaning, scarcely modify the above numerical predictions. Similarly, the specific energy fracture in Mode IIa, G_F^{IIa}; whether divided by 2 or to multiplied by 100, produces very close P–displacement and P–CMOD curves. This is because in this geometry of mixed mode fracture, the crack grows under stable local Mode I, and its growth is only slightly affected by the modification of the Mode II governing variables, whenever they move into a range with physical meaning. Fig. 14 shows the numerical predictions of load P–CMOD curves of the Type 1 tests with $G_F^{IIa}=0.5$, 1, 10 and 100 G_F.

4.1.2. Comparison with the experiments by Arrea and Ingraffea

The experimental results published by Arrea and Ingraffea [32] are traditionally used to verify normal/shear cracking of concrete models. This pioneering work on mixed mode fracture of concrete is a standard for numerical and analytical fracture models.

The only material properties measured in the tests by Arrea and Ingraffea [32] are the compressive strength, f_c, the Young's modulus, E, and the Poisson's ratio, ν. There are no

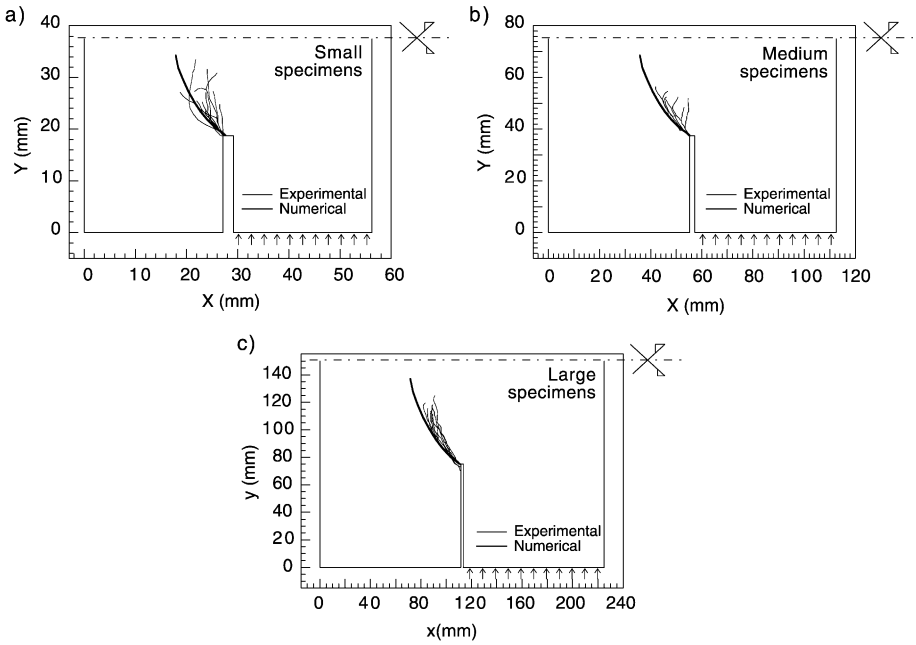

Fig. 21. Experimental envelopes and numerical predictions of the crack trajectories of the tests of Gálvez et al. [36]: (a) small specimens ($2h=75$ mm); (b) medium specimens ($2h=150$ mm); (c) large specimens ($2h=300$ mm).

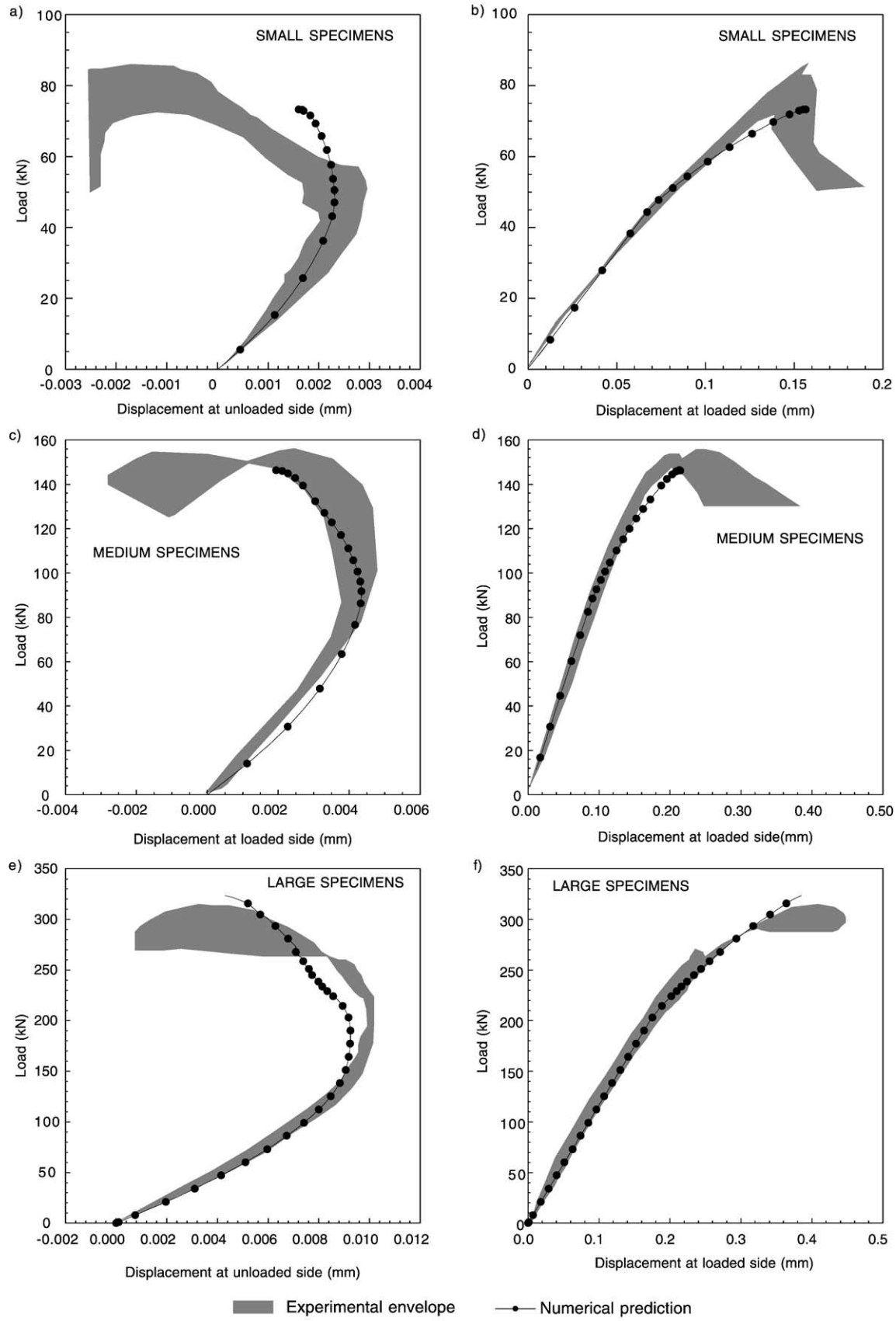

Fig. 22. Experimental envelopes and numerical predictions of the tests of Gálvez et al. [36].

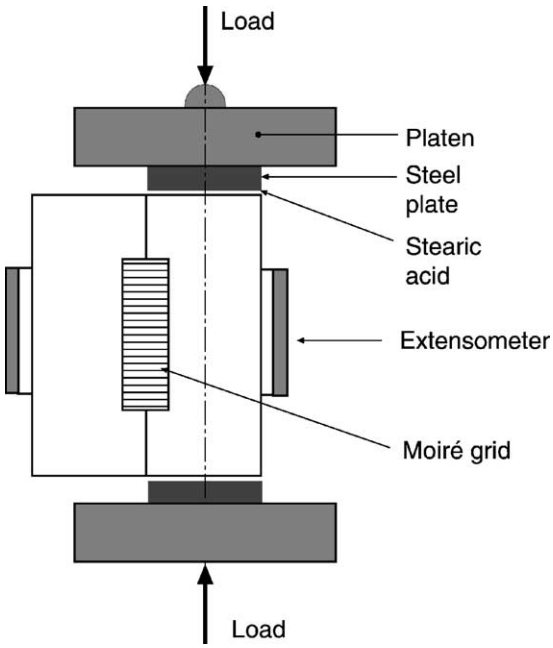

Fig. 23. Geometry and testing arrangement of the tests of Cedolin et al. [35].

data about the tensile strength, f_{t_0}, or the specific energy fracture, G_F, both essential to defining the softening curve. Saleh and Aliabadi [28] validated their numerical model by taking $f_{t_0}=2.8$ and $G_F=100$ N/m. Xie and Gerstle, for the same set of tests took $f_{t_0}=4.0$ MPa and $G_F=150$ N/m; obviously, the concrete fracture parameters are quite different. A relatively small number of beams were tested in each series. Mortar tests (Series A): two beams, only one valid test. Concrete tests: Series B, three beams, all valid; and Series C three beams, only two valid. A wide experimental scatter band is shown in [32] for the crack paths and the load–crack mouth sliding displacement (CMSD) curves. These inconveniences suggest that a complementary set of experimental data is needed for an objective validation of the mixed mode cracking models.

Fig. 15 shows the geometry, forces and boundary conditions of the tests of Arrea and Ingraffea [32]. The notch depth, a, was 70 mm in Series A beams and 82.4 mm in Series B and C. The thickness of the beams was 102 mm for Series A and 152 mm for Series B and C. Table 2 shows the material properties; the values of the tensile strength, f_{t_0}, and the specific fracture energy, G_F, are estimated from the material properties in Ref. [32] and the recommendations of the Model Code [52]. Complementary parameters for the model were estimated: $c=5.0$ MPa, $\phi_f=0.5$ rad, $\phi_d=0.3$ rad and $G_F^{IIa}=4/3G_F^I$.

Fig. 16 compares the experimental crack paths and the numerical prediction for Series A, B and C and shows that the numerical model gives a good approximation to the experimental crack path.

Fig. 17 shows a deformed mesh used to study the mixed mode fracture behaviour of the B test series of Arrea and Ingraffea [32].

Fig. 18 shows the experimental envelope and the numerical predictions of the load P–CMSD curves. The numerical results are within the experimental scatter band.

Fig. 19 shows the numerical predictions of load P–CMSD of the Series B with $G_F^{IIa}=0.5$, 1, 10 and 100 G_F. The comments made above for the tests of Gálvez et al. [30] in relation to the influence of the Mode II parameters in the load P–CMOD curves are valid for the load P–CMSD curves of Arrea and Ingaffea [32].

4.2. Double-edge notched specimens under compression loading

A novel testing procedure for pure Mode II fracture of concrete was recently proposed by Reinhardt et al. [33,34]: the double-edge notched specimen under compression loading of one half specimen. The test procedure was used by other researchers [35,36]. Fig. 20 shows a sketch of the tests by Gálvez et al. [36]. The procedure, based on the Tada et al. [53] theoretical solution for a Mode II problem of an infinite plate, assumes that the crack is vertically developed along the ligament under pure Mode II of fracture. Experimental results [36] and numerical simulations [54] have shown that the crack grows into the unloaded half specimen under mixed mode (Modes I and II) fracture.

Two failure processes are at work during the test: crack growth from the notches running along the ligament (cracking) and compression failure of the loaded part (crushing). For our purpose, the main important question is that the specimen fails under compression loading (crushing), and the numerical modelling of the compression failure is important to simulate the whole test. However, the nucleation and growth process of the mixed mode cracks up to the failure compression is adequate to verify the mixed mode fracture model. Detailed modelling of compression failure is beyond the scope of this paper. The Drucker–Prager model, included in the ABAQUS© materials library, is used to model this behaviour.

The experimental results developed by Gálvez et al. [36] and by Cedolin et al. [35] are adopted for verification of the mixed mode fracture model.

4.2.1. Comparison with the experiments by Gálvez et al.

Fig. 20 shows the testing arrangement of the double-edge specimens of concrete under compression loading of Gálvez et al. [36]. The dimensions and number of specimens are detailed in Table 3. Three homothetic specimen sizes were tested. The mechanical properties of the concrete, measured

Table 4
Dimensions of the specimens and number of tests by Cedolin et al. [35]

Specimen	Height, $2h$ (mm)	Length, $2w$ (mm)	Ligament, $2a$ (mm)
H60	60	45	30
H120	120	90	60
H240	240	180	120

Thickness: 6 mm.

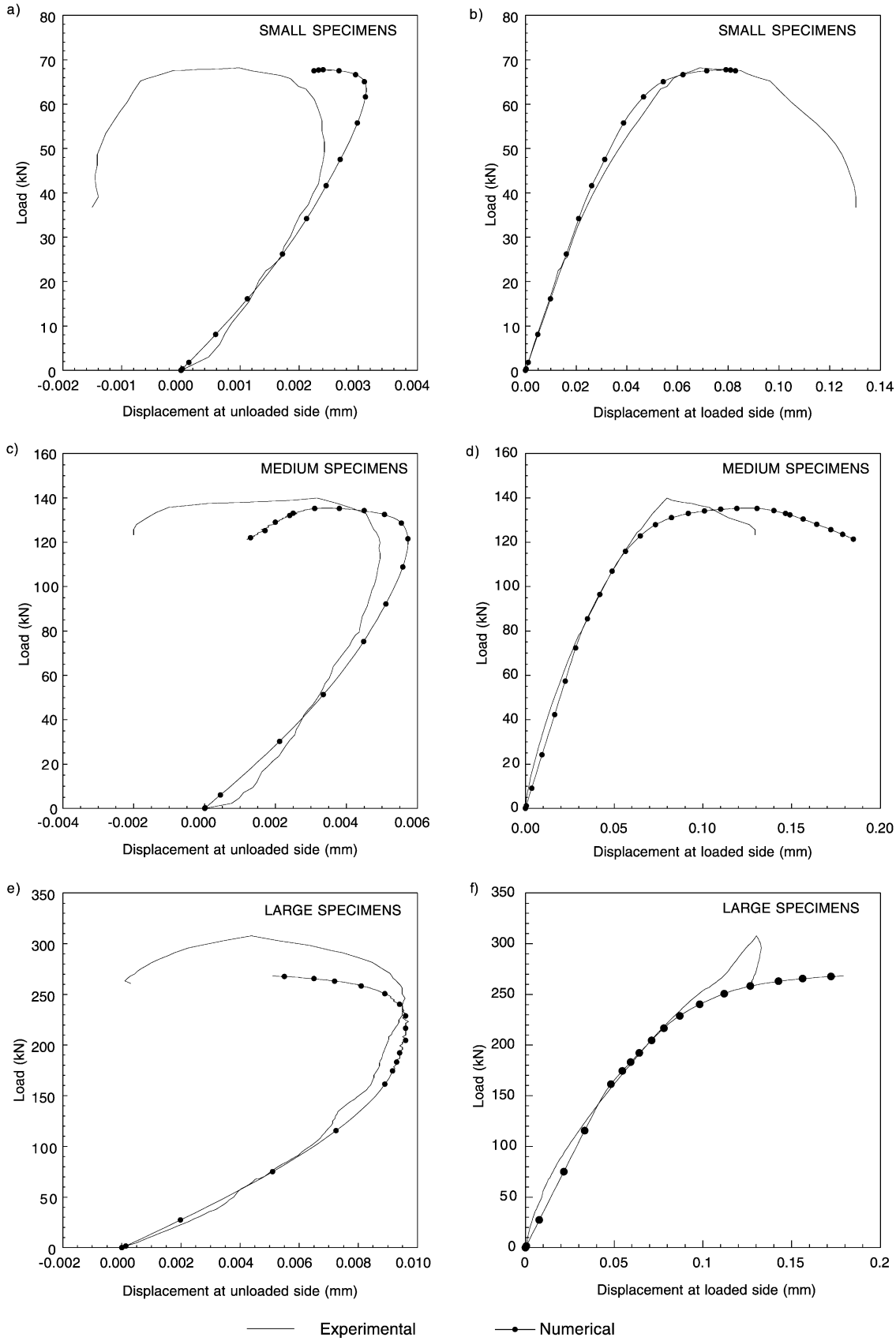

Fig. 24. Experimental envelopes and numerical predictions of the test of Cedolin [35].

according to ASTM C 39 [50], ASTM C 496 [39], ASTM C 469 [51] and RILEM 50-FMC [40], were respectively: $f_c = 57$ MPa, $f_{t_0} = 3.0$ MPa, $E = 38$ GPa and $G_F = 69$ N/m. Complementary parameters of the model were estimated: $c = 5.0$ MPa, $\phi_f = 0.5$ rad, $\phi_d = 0.4$ rad and $G_F^{IIa} = 115$ N/m.

Fig. 21 compares the experimental tests and numerical prediction of the crack paths for the three sizes of specimen and shows that the numerical model is a good approximation of the experimental crack path.

Fig. 22a, c and e shows the experimental envelope and the numerical prediction of the load versus displacement recorded by the extensometer placed on the unloaded half part of the specimen (left extensometer in Fig. 20) for the three sizes of specimen. The nucleation and growth of the cracks is shown in the curves by the loss of linearity and a marked drawing back. The crack growth moderates the load transference from the loaded to the unloaded part of the specimen and leads to a reduction in the shortening of the unloaded part.

Fig. 22b, d and e shows the experimental envelope and the numerical prediction of the load versus displacement recorded by the extensometer placed on the loaded half of the specimen (right extensometer in Fig. 20) for the three specimen sizes. The numerical prediction stops at the peak load. The numerical modelling of the post peak behaviour under compression loading needs an adequate compression model, beyond the scope of this work. Numerical prediction up to the peak load is good.

As shown in Fig. 22, the nonlinear behaviour of the loaded part up to peak load is of minor importance in the fracture behaviour of the unloaded part. This confirms the availability of this testing procedure to verify the numerical and analytical models of mixed mode fracture of quasi-brittle materials.

4.2.2. Comparison with the experiments by Cedolin et al.

Fig. 23 shows the arrangement for the tests developed by Cedolin et al. [35]. The dimensions are detailed in Table 4. Three homothetic specimen sizes were tested. The material properties adopted for the numerical simulation were: $f_{t_0} = 5.0$ MPa, $E = 30$ GPa and $G_F = 80$ N/m, $c = 6.0$ MPa, $\phi_f = 0.5$ rad, $\phi_d = 0.4$ rad and $G_F^{IIa} = 96$ N/m.

Fig. 24 shows the experimental results and the numerical prediction of the load versus displacement of the extensometers placed on the loaded and unloaded part of the specimens for the three sizes of specimen. In all cases, the numerical prediction adequately fits the experimental records. The comments made above for the tests of Gálvez et al. [36] in relation to the form of the curves are valid for the curves of Cedolin et al. [35].

5. Summary and final remarks

A numerical procedure for mixed mode fracture of quasi-brittle materials is presented, which predicts the crack path based on the LEFM. The mixed mode cohesive model is an extension of the Mode I cohesive model to mixed mode fracture using the formulation of classical plasticity. The model is introduced into a commercial finite element code by an user subroutine and experimentally contrasted. The numerical results agree quite well with two experimental sets of mixed mode fracture tests. Two more experimental sets of mixed mode fracture based on the double-edge notched testing arrangement were simulated, also with good agreement. It is worth noting that the numerical prediction is based on the usual material properties, previously measured by standard methods, and the numerical model predicts the experimental curves of the load versus displacement of the several control points of the specimens of three sizes.

The influence of the Mode IIa fracture energy, G_F^{IIa}, is studied by modifying their values in a wide range. For the notched beams, dividing by 2 or multiplying by 100 the specific fracture energy in Mode IIa, G_F^{IIa}, produces very close load P–CMSD, P–CMOD and load P–displacement curves in all cases fitted in the experimental scatter band. These curves, corresponding to notched beams, are coincident for $G_F^{IIa} = 10$ and 100 times G_F^I and are scarcely different from the curves with $G_F^{IIa} = G_F^I$. Only the curves with $G_F^{IIa} = 0.5 G_F^I$ show a small difference. Even though no experimental tests have shown values of G_F^{IIa} smaller than G_F^I, the halved value was included to give a wider range of Mode II parameters. These results suggest that, for these geometries of mixed mode fracture, the crack growth is only slightly affected by the modification of the Mode IIa fracture energy, G_F^{IIa}, whenever they fit into a wide range with physical meaning. Further research about the influence of the parameters of Mode II in the mixed Mode I/II fracture of concrete would be welcomed.

Acknowledgments

The authors gratefully acknowledge the financial support for this research provided by the Ministerio de Educación y Cultura under grants PB97-0579, MAT2001-3863-C03-02, 1FD97-1641 and EVK4-2001-00091, and by the complementary financial support provided by the Universidad de Castilla La Mancha and the Junta de Comunidades de Castilla La Mancha.

Appendix A. Interface element formulation

The formulation of the interface element starts from the internal energy, calculated as the integral of the stresses multiplied by the conjugated strains. In an interface element, the stress is constant for a fixed crack opening, which is expressed as follows (Eq. (A.1)):

$$dW_{int} = \boldsymbol{u}^T \boldsymbol{t} dA \tag{A.1}$$

where $dA = e\,dl$, and e is the thickness and dl is the differential length of the element.

The displacements inside the element are obtained by interpolation of the nodal displacements. Fig. 8 shows that the interface elements have couples of nodes, which are coincident in the undeformed element. The form functions adopted are linear and quadratic, in accordance with the type of element. For two-dimensional problems, these elements have only the longitudinal dimension. Then the formulation of the linear element is presented. The form functions are as follows (Eq. (A.2)):

$$N_1 = \frac{1}{2}(1+\xi); \quad N_2 = \frac{1}{2}(1-\xi) \tag{A.2}$$

with ξ is between -1 and 1.

In accordance with the nodal numeration of Fig. 8, and knowing that the relative displacement between the faces of the element is calculated from the relative displacement of opposite nodes, the following nodal displacement vector is adopted, $\mathbf{d}_{el}$ (Eq. (A.3)):

$$\mathbf{d}_{el}^{\mathrm{T}} = [u_1\ v_1\ u_2\ v_2\ u_3\ v_3\ u_4\ v_4] \tag{A.3}$$

where u_i and v_i are the displacements of the i node in directions normal and tangential to the crack face.

The relative displacement vector inside the interface element is obtained by interpolation (Eq. (A.4)):

$$\boldsymbol{u}(\xi) = \begin{bmatrix} u(\xi) \\ v(\xi) \end{bmatrix} = \begin{bmatrix} -N_1 & 0 & -N_2 & 0 & N_1 & 0 & N_2 & 0 \\ 0 & -N_1 & 0 & -N_2 & 0 & N_1 & 0 & N_2 \end{bmatrix} \mathbf{d}_{el} \tag{A.4}$$

and the $\mathbf{B}$ matrix, according to classic terminology, is expressed as follows (Eq. (A.5)):

$$\mathbf{B} = \begin{bmatrix} -N_1 & 0 & -N_2 & 0 & N_1 & 0 & N_2 & 0 \\ 0 & -N_1 & 0 & -N_2 & 0 & N_1 & 0 & N_2 \end{bmatrix} \tag{A.5}$$

The internal forces are obtained by the virtual works theorem (Eq. (A.6)):

$$\boldsymbol{f}_{\mathrm{int}} = \int_l \mathbf{B}(x)^{\mathrm{T}} \boldsymbol{t}\, e\, dl = e \int_l \mathbf{B}(x)^{\mathrm{T}} \boldsymbol{t}\, dl \tag{A.6}$$

and naming L to the length of the element:

$$f_{\mathrm{int}} = e\frac{L}{2}\int_{-1}^{1} \mathbf{B}(\xi)^{T} \boldsymbol{t}\, d\xi \tag{A.7}$$

Once the nodal forces are known, the contribution of each element to the tangent matrix is evaluated. Based on the incremental expression of Eq. (A.7), we have Eq. (A.8):

$$\Delta \boldsymbol{f}_{\mathrm{int}} = e\frac{L}{2}\int_{-1}^{1} \mathbf{B}(\xi)^{\mathrm{T}} \Delta \boldsymbol{t}\, d\xi \tag{A.8}$$

and remembering Eq. (25), we have Eq. (A.9):

$$\Delta \boldsymbol{f}_{\mathrm{int}} = e\frac{L}{2}\left(\int_{-1}^{1} \mathbf{B}(\xi)^{\mathrm{T}} \boldsymbol{C}^{\mathrm{ep}} \mathbf{B}(\xi)\, d\xi\right) \Delta \mathbf{d}_{el} \tag{A.9}$$

where the contribution of each element to the tangent matrix is:

$$\boldsymbol{K}_{el} = e\frac{L}{2}\int_{-1}^{1} \mathbf{B}(\xi)^{\mathrm{T}} \boldsymbol{C}^{\mathrm{ep}} \mathbf{B}(\xi)\, d\xi \tag{A.10}$$

The interface element formulation is ready for incorporation into a finite element code.

References

[1] M. Elices, J. Planas, Material models, in: L. Elfgren (Ed.), Fracture Mechanics of Concrete Structures, Chapman & Hall, London, 1989, pp. 16–66.

[2] E. Schlangen, J.G. Van Mier, Mixed-mode fracture propagation: a combined numerical and experimental study, in: H.P. Rossmanith (Ed.), Fracture and Damage of Concrete and Rock, E & FN Spon, London, 1993, pp. 166–175.

[3] Z.P. Bažant, J. Planas, Fracture and Size Effect in Concrete and Other Quasibrittle Materials, CRC Press, New York, 1998.

[4] Y. Rashid, Analysis of prestressed concrete pressure vessels, Nuclear Engineering and Design, Balkema, Rotterdam, 1968, pp. 265–286.

[5] V. Červenka, Inelastic finite element analysis of reinforced concrete panels under in-plane loads, PhD thesis, University of Colorado, 1970.

[6] M. Suidan, W. Schnobrich, Finite element analysis of reinforced concrete, J. Struct. Div. ASCE 99 (1973) 2109–2122.

[7] R. Cope, P. Rao, L. Clark, P. Norris, Modelling of reinforced concrete behaviour for finite element analysis of bridge slabs, in: C. Taylor (Ed.), Numerical Methods for Non-linear Problems, Pineridge Press, Swansea, 1980, pp. 457–470.

[8] A. Gupta, H. Akbar, Cracking in reinforced concrete analysis, J. Struct. Eng. ASCE 110 (1984) 1735–1746.

[9] K. Willam, E. Pramono, S. Stur, Fundamental issues of smeared crack models, in: S.P. Shah, S.E. Swartz (Eds.), Proceedings of the SEM-RILEM International Conference on Fracture of Concrete and Rock, SEM, Springer-Verlag, New York, 1987, pp. 192–207.

[10] R. de Borst, P. Nauta, Non-orthogonal cracks in a smeared finite element model, Eng. Comput. 2 (1985) 35–46.

[11] J. Rots, Computational modelling of concrete fracture, PhD thesis, Delft University, 1988.

[12] R. Hill, Bifurcation and uniqueness in non-linear mechanics continua, Problems in Continuum Mechanics, SIAM, Society for Industrial and Applied Mathematics, Philadelphia, Pennsylvania, 1961, pp. 155–164.

[13] J. Mandel, Conditions de stabilité et postulat de Drucker, Rheology and Soil Mechanics, IUTAM Symposium, Springer-Verlag, Berlin, 1964, pp. 56–68.

[14] I. Carol, P. Prat, M. López, Normal/shear cracking model: Application to discrete crack analysis, J. Eng. Mech. ASCE 123 (1997) 765–773.

[15] Z.P. Bažant, B. Oh, Crack band theory for fracture of concrete, Mater. Struct. 16 (1983) 155–177.

[16] K. Willam, Experimental and computational aspects of concrete fracture, in: F. Damjanic, et al. (Eds.), Computer Aided Analysis and Design of Concrete Structures, Pineridge Press, Swansea, 1984, pp. 33–70.
[17] J. Rots, P. Nauta, G. Kursters, J. Blaauwendraad, Smeared crack approach and fracture localization in concrete, Heron 30 (1985) 1–48.
[18] Z.P. Bažant, G. Pijaudier-Cabot, Nonlocal continuum damage, localization, stability and convergence, J. Appl. Mech. 55 (1988) 287–293.
[19] Z.P. Bažant, J. Ožbolt, Nonlocal microplane for fracture, damage and size effect in structures, J. Eng. Mech. ASCE 116 (1990) 2485–2504.
[20] R. de Borst, H. Mühlhaus, Gradient dependent plasticity: Formulation and algorithmic aspects, Int. J. Numer. Methods Eng. 35 (1992) 521–539.
[21] P. Steinmann, K. Willam, Finite element analysis of elastoplastic discontinuities, J. Struct. Div. ASCE 120 (1994) 2428–2442.
[22] A. Hillerborg, M. Modéer, P. Petersson, Analysis of crack formation and crack growth in concrete by means of fracture mechanics and finite elements, Cem. Concr. Res. 6 (1976) 773–782.
[23] J. Červenka, Discrete Crack Modelling in Concrete Structures, PhD thesis, University of Colorado, 1994.
[24] R. Reich, J. Červenka, V. Saouma, MERLIN: A three-dimensional finite element program based on a mixed iterative solution strategy for problems in elasticity, plasticity, linear and nonlinear fracture mechanics, Technical Report, Department of Civil Engineering, University of Colorado, Boulder, and Electric Power Research Institute, Palo Alto, CA, 1997.
[25] M. Xie, W. Gerstle, Energy-based cohesive crack propagation modeling, J. Eng. Mech. 121 (1995) 1349–1358.
[26] R. Reich, G. Plizzari, J. Červenka, V. Saouma, Implementation and validation of a nonlinear fracture model in 2D/3D finite element code, in: F.H. Wittmann (Ed.), Numerical Models in Fracture Mechanics, Balkema, Rotterdam, 1991, pp. 265–287.
[27] S. Valente, On the cohesive crack model in mixed-mode conditions, Fracture of Brittle Disordered Materials, Concrete, Rock and Ceramics, E & FN Spon, London, 1995, pp. 66–80.
[28] A. Saleh, M. Aliabadi, Crack growth analysis in concrete using boundary element method, Eng. Fract. Mech. 51 (1995) 533–545.
[29] J. Červenka, J.M. Chandra, V. Saouma, Mixed mode fracture of cementitious bimaterial interfaces: Part II. Numerical simulation, Eng. Fract. Mech. 60 (1998) 95–107.
[30] J.C. Gálvez, M. Elices, G.V. Guinea, J. Planas, Mixed mode fracture of concrete under proportional and nonproportional loading, Int. J. Fract. 94 (1998) 267–284.
[31] D.A. Cendón, J.C. Gálvez, M. Elices, J. Planas, Modelling the fracture of concrete under mixed loading, Int. J. Fract. 103 (2000) 293–310.
[32] M. Arrea, A. Ingraffea, Mixed Mode Crack Propagation in Mortar and Concrete, Report 81-13, Department of Structural Engineering, Cornell University, 1982.
[33] H.W. Reinhardt, S. Xu, Experimental determination of K_{IIc} of normal strength concrete, Mater. Struct. 31 (1998) 296–302.
[34] H.W. Reinhardt, J. Ožbolt, S. Xu, A. Dinku, Shear of structural concrete members and pure mode II testing, Adv. Cem. Based Mater. 5 (1997) 75–85.
[35] L. Cedolin, G. Bisi, P.A. Nardello, Mode II fracture resistance of concrete, Concr. Sci. Eng. RILEM 1 (1999) 1–9.
[36] J.C. Gálvez, M. Elices, D.A. Cendón, Fracture of double-edge notched specimens of concrete under compression loading, Construction Materials: Theory and Application, Ibidem-Verlag, Stuttgart, 2000, pp. 95–105.
[37] Z.P. Bažant, J.K. Kim, P.A. Pfeiffer, Non linear fracture properties from size effect tests, J. Struct. Eng. ASCE 112 (1986) 289–307.
[38] A. Carpinteri, Cracking of strain-softening materials, in: M.H. Aliabadi, et al. (Eds.), Static and Dynamic Fracture Mechanics, Computational Mechanics Publications, Southampton, 1994, pp. 311–365.
[39] ASTM C 496-96, Standard method for splitting tensile strength of cylindrical concrete specimens, Annual Book of ASTM Standards, ASTM 4.02, 1999, pp. 266–269.
[40] RILEM, 50-FMC Committee on Fracture Mechanics of Concrete, Determination of the fracture energy of mortar and concrete by means of three-point bend tests of notched beams, Matér. Constr. 18 (1986) 285–290.
[41] V. Gopalaratnam, S. Shah, Softening response of plain concrete in direct tension, Struct. J. ACI 82 (1985) 310–323.
[42] H. Cornelissen, D. Hordijk, H. Reinhardt, Experimental determination of crack softening characteristics of normal weight and lightweight concrete, Heron 31 (1986) 45–56.
[43] J. Planas, M. Elices, Towards a measure of G_F: an analysis of experimental results, in: F.H. Wittmann (Ed.), Fracture Toughness and Fracture Energy of Concrete, Elsevier, Amsterdam, 1986, pp. 381–390.
[44] H. Reinhardt, Fracture mechanics of fictitious crack propagation in concrete, Heron 29 (1984) 3–42.
[45] F. Erdogan, G.C. Sih, On the crack extension in plates under plane loading and transverse shear, J. Basic Eng. 85 (1963) 519–527.
[46] D. Broek, Elementary Engineering Fracture Mechanics, Martinus Nijhoff Publishers, Dordrecht, 1986, pp. 374–380.
[47] P. Wawryzynek, A. Ingraffea, FRANC2D: A Two-Dimensional Crack-Propagation Simulator, Version 2.7.
[48] J.C. Gálvez, M. Elices, G.V. Guinea, J. Planas, Crack trajectories under mixed mode and non-proportional loading, Int. J. Fract. 81 (1996) 171–193.
[49] R.V. Mahajan, K. Ravi-Chandar, An experimental investigation of mixed-mode fracture, Int. J. Fract. 41 (1989) 235–252.
[50] ASTM C 39-96, Standard method for compressive strength of cylindrical concrete specimens, Annual Book of ASTM Standards, ASTM 4.02, 1999, pp. 18–22.
[51] ASTM C 469-96, Standard method for static modulus of elasticity and Poisson's ratio of concrete in compression, Annual Book of ASTM Standards, ASTM 4.02, 1999, pp. 241–244.
[52] CEB-FIP, Model Code 1990, Lausanne, 1991.
[53] H. Tada, P. Paris, G. Irwin, The Stress Analysis of Cracks Handbook, second ed., Paris Productions, St. Louis, 1985, p. 4.13.
[54] M. di Prisco, L. Ferrara, On the evaluation of mode II fracture energy in high strength concrete, in: R. de Borst, N. Bićanić, H. Mang, G. Meschkeeds (Eds.), Computational Modelling of Concrete Structures, Balkema, Rotterdam, 1998, pp. 409–418.